7-2010

Sparse x-ray CT image reconstruction using ECME hard thresholding methods

Kun Qiu
Iowa State University

Aleksandar Dogandžić
Iowa State University, ald@iastate.edu

Sparse x-ray CT image reconstruction using ECME hard thresholding methods

Abstract
We apply expectation-conditional maximization either (ECME) hard thresholding algorithms to X-ray computed tomography (CT) reconstruction, where we implement the sampling operator using the nonuniform fast Fourier transform (NUFFT). The measurements follow an underdetermined linear model, where the regression-coefficient vector is a sum of an unknown deterministic sparse signal component and a zero-mean white Gaussian component with an unknown variance. Our ECME schemes aim at maximizing this model's likelihood function with respect to the sparse signal and variance of the random signal component. These schemes exploit signal sparsity in the discrete wavelet transform (DWT) domain and yield better reconstructions than the traditional filtered backprojection (FBP) approach, which is demonstrated via numerical examples. In contrast with FBP, our methods achieve artifact-free reconstructions in undersampled and limited-angle projection examples. We also compare the ECME schemes with a state-of-the-art convex sparse signal reconstruction approach in terms of the reconstruction speed.

Keywords
image reconstruction, acoustic signal processing, image resolution, data acquisition, nondestructive evaluation, QNDE, Electrical and Computer Engineering

Disciplines
Electrical and Computer Engineering | Materials Science and Engineering | Structures and Materials

This article appeared in *AIP Conference Proceedings* 1335 (2011): 469–476 and may be found at http://dx.doi.org/10.1063/1.3591889.

SPARSE XRAY CT IMAGE RECONSTRUCTION USING ECME HARD THRESHOLDING METHODS

Kun Qiu and Aleksandar Dogandžić

Citation: AIP Conf. Proc. **1335**, 469 (2011); doi: 10.1063/1.3591889
View online: http://dx.doi.org/10.1063/1.3591889
View Table of Contents: http://proceedings.aip.org/dbt/dbt.jsp?KEY=APCPCS&Volume=1335&Issue=1
Published by the American Institute of Physics.

SPARSE X-RAY CT IMAGE RECONSTRUCTION USING ECME HARD THRESHOLDING METHODS

Kun Qiu and Aleksandar Dogandžić

Iowa State University, Center for Nondestructive Evaluation,
1915 Scholl Road, Ames, IA 50011, USA

ABSTRACT. We apply expectation-conditional maximization either (ECME) hard thresholding algorithms to X-ray computed tomography (CT) reconstruction, where we implement the sampling operator using the nonuniform fast Fourier transform (NUFFT). The measurements follow an underdetermined linear model, where the regression-coefficient vector is a sum of an unknown deterministic sparse signal component and a zero-mean white Gaussian component with an unknown variance. Our ECME schemes aim at maximizing this model's likelihood function with respect to the sparse signal and variance of the random signal component. These schemes exploit signal sparsity in the discrete wavelet transform (DWT) domain and yield better reconstructions than the traditional filtered backprojection (FBP) approach, which is demonstrated via numerical examples. In contrast with FBP, our methods achieve artifact-free reconstructions in undersampled and limited-angle projection examples. We also compare the ECME schemes with a state-of-the-art convex sparse signal reconstruction approach in terms of the reconstruction speed.

Keywords: Compressive Sampling, Expectation-Conditional Maximization Either (ECME) Algorithm, Sparse Signal Reconstruction, Successive Overrelaxation, Unconstrained Sparsity Selection, X-Ray Computed Tomography (CT)
PACS: 81.70.Tx Computed tomography

INTRODUCTION

Sparse signal reconstruction and compressive sampling theory and methods are built upon the fact that most signals in the real world are *sparse* or *nearly sparse* in some transform domain [1]–[4]. Specifically, for an $m \times 1$ vector $\boldsymbol{x}$ representing the $m_1 \times m_2$ image (obtained by stacking the image into a column vector for notational convenience, where $m = m_1\, m_2$) and an appropriate $m \times m$ orthogonal *sparsifying transform matrix* Ψ, we have

$$\boldsymbol{x} = \Psi\, \boldsymbol{s} \tag{1}$$

where $\boldsymbol{s}$ is an $m \times 1$ transform-coefficient vector with most elements having negligible magnitudes. Here, we choose Ψ to be the inverse discrete wavelet transform (DWT) matrix; consequently, $\boldsymbol{s}$ is the wavelet-coefficient vector of the image $\boldsymbol{x}$. The idea behind compressive sampling is to directly *sense* the non-negligible components of $\boldsymbol{s}$ using a small number of linear measurements:

$$\boldsymbol{y} = \Phi\, \boldsymbol{x} = \Phi\, \Psi\, \boldsymbol{s} \stackrel{\triangle}{=} H\, \boldsymbol{s} \tag{2}$$

Review of Progress in Quantitative Nondestructive Evaluation, Volume 30
AIP Conf. Proc. 1335, 469-476 (2011); doi: 10.1063/1.3591889

where $\boldsymbol{y}$ is an $N \times 1$ measurement vector, Φ is a known $N \times m$ *sampling matrix* with

$$N \leq m \tag{3}$$

and $H = \Phi\, \Psi$ is the $N \times m$ *sensing matrix*. We note that only Φ is employed in the data collection (sampling) process, whereas Ψ and H are needed only for the image reconstruction. The compressive sampling theory asserts that it is possible to accurately recover the sparse or compressible signal coefficient vector $\boldsymbol{s}$ from the measurements $\boldsymbol{y}$ *provided that* the sampling matrix Φ is *incoherent* with the sparsifying transform matrix Ψ [3]. In simple words, this incoherence implies that each measurement incorporates information from almost all sparse signal coefficients (i.e. significant elements of $\boldsymbol{s}$). For example, if we uniformly sample a signal that is sparse in time at a low (below-Nyquist) rate, we will miss the spikes in the signal and, will therefore not be able to recover it; this is because the sampling and sparsity bases are the same and therefore coherent. Incoherent data collection often requires new hardware design, such as single-pixel camera, which uses a single-pixel detector instead of a photodetector array for imaging in visible light [5] or in the terahertz frequency range [6]. Interestingly, X-ray computed tomography (CT) is an exception: existing X-ray CT systems can be directly applied to collect compressive samples that approximately satisfy the incoherence assumption. This is due to the fact that the CT measurements are inherently linear combinations of the wavelet coefficients of the underlying image [7, Ch. 4.1] (see also the following discussion), where the incoherence with the sparsity basis can be approximately achieved simply by taking measurements at equally spaced angles.

The Fourier slice theorem [7, Ch. 3.2] states that the 1-D Fourier transform of a parallel X-ray projection coincides with the 2-D discrete-space Fourier transform (DSFT) of the underlying image along the radial straight line in the 2-D spatial frequency plane that passes through the origin at the projection angle. Therefore, the measurements $\boldsymbol{y}$ in (2) are the samples of this 2-D DSFT taken along the projection angles[1]; consequently, each row of the sampling matrix Φ consists of the real or imaginary parts of the m Fourier weights:

$$\exp[-j\,(\omega_1\, n_1 + \omega_2\, n_2)], \quad n_1 = 1, 2, \ldots, m_1,\ n_2 = 1, 2, \ldots, m_2 \tag{4}$$

needed to determine the 2-D DSFT at the spatial frequency (ω_1, ω_2) corresponding to the appropriate element of $\boldsymbol{y}$.

Even though the effectiveness of compressive sampling for X-ray CT reconstruction has been reported in e.g. [1], [2], [8], and [9], these references contain only simulated examples with synthetic images such as the Shepp-Logan phantom, where the X-ray CT measurements are approximated by a collection of 2-D discrete Fourier transform (DFT) coefficients of the underlying image on the uniform Cartesian grid in the 2-D spatial frequency plane. The actual CT measurements lie on straight radial lines in the 2-D spatial frequency plane and are therefore concentrated in the center (low-frequency) region of this plane, see Fig. 1. Therefore, the approximation of the CT measurements by the 2-D DFT coefficients in [1], [2], [8], and [9] is crude and does not accurately represent real X-ray CT data collection.

In this paper, we apply our expectation-conditional maximization either (ECME) hard thresholding algorithms in [8] and [9] to solve the X-ray CT reconstruction problem, where we employ the realistic non-uniform frequency-domain sampling pattern. We first review our probabilistic measurement model and ECME algorithms and then apply these algorithms to reconstruct images from real X-ray CT measurements of an industrial object. The proposed algorithms are compared with the state-of-the-art approaches in terms of the reconstruction performance and speed.

[1]Here, we consider the real and imaginary parts of the 2-D DSFT samples separately.

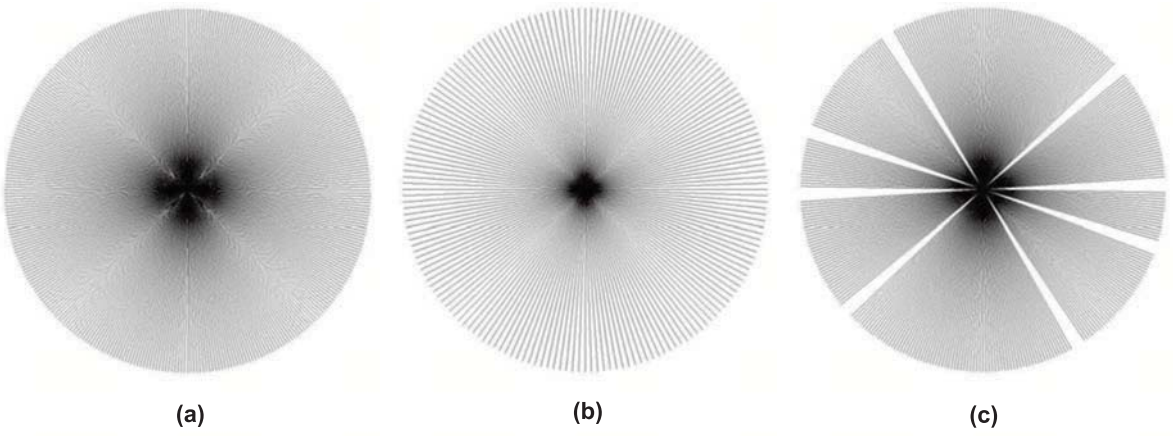

FIGURE 1. The frequency sampling patterns for: (a) 180 uniform-angle projections, (b) 90 uniform-angle projections, and (c) 164 limited-angle projections.

We introduce the notation used in this paper: $\mathcal{N}(\boldsymbol{y}\,;\,\boldsymbol{\mu},\Sigma)$ denotes the multivariate probability density function (pdf) of a real-valued Gaussian random vector $\boldsymbol{y}$ with mean vector $\boldsymbol{\mu}$ and covariance matrix Σ; $|\cdot|$, $\|\cdot\|_{\ell_p}$, $\det(\cdot)$, "^{T}" denote the absolute value, ℓ_p norm, determinant, and transpose, respectively; the smallest integer larger than or equal to a real number x is $\lceil x \rceil$; I_n, $\mathbf{0}_{n\times 1}$, and $0_{n\times m}$ are the identity matrix of size n, the $n \times 1$ vector of zeros, and the $n \times m$ matrix of zeros, respectively; $\dim(A)$ denotes the size of a set A; $\mathrm{supp}(\boldsymbol{x})$ returns the support set of a vector $\boldsymbol{x}$, i.e. the index set corresponding to the nonzero elements of $\boldsymbol{x}$, e.g. $\mathrm{supp}([0,1,-5,0,3,0]^T) = \{2,3,5\}$; the thresholding operator $\mathcal{T}_r(\boldsymbol{x})$ keeps the r largest-magnitude elements of a vector $\boldsymbol{x}$ intact and sets the rest to zero, e.g. $\mathcal{T}_2([0,1,-5,0,3,0]^T) = [0,0,-5,0,3,0]^T$.

We refer to an $N \times m$ sensing matrix H as *proper* if it has full rank and satisfies (3), which implies that the rank of H is equal to N. Throughout this paper, we assume that sensing matrices H are proper, which is satisfied in almost all practical sparse signal reconstruction scenarios.

PROBABILISTIC MODEL AND THE ECME ALGORITHMS

We model a $N \times 1$ real-valued measurement vector $\boldsymbol{y}$ as

$$\boldsymbol{y} = H\,\boldsymbol{z} \tag{5a}$$

where H is an $N \times m$ real-valued proper sensing matrix, $\boldsymbol{z}$ is an $m \times 1$ multivariate Gaussian vector with pdf

$$p_{\boldsymbol{z}\,|\,\boldsymbol{\theta}}(\boldsymbol{z}\,|\,\boldsymbol{\theta}) = \mathcal{N}(\boldsymbol{z}\,|\,\boldsymbol{s},\sigma^2\,I_m) \tag{5b}$$

$\boldsymbol{s} = [s_1, s_2, \ldots, s_m]^T$ is an *unknown* $m \times 1$ real-valued sparse signal vector containing *at most* r nonzero elements ($r \leq m$), and σ^2 is an unknown *variance-component parameter*; we refer to r as the *sparsity level* of the signal and to the signal $\boldsymbol{s}$ as being *r-sparse*. Note that $\|\boldsymbol{s}\|_{\ell_0} = \dim(\mathrm{supp}(\boldsymbol{s}))$ counts the number of nonzero elements in $\boldsymbol{s}$; we refer to $\|\boldsymbol{s}\|_{\ell_0}$ as the *support size* of $\boldsymbol{s}$. Therefore, the support size $\|\boldsymbol{s}\|_{\ell_0}$ of a r-sparse vector $\boldsymbol{s}$ is less than or equal to r.

The set of unknown parameters is

$$\boldsymbol{\theta} = (\boldsymbol{s},\sigma^2) \in \Theta_r \tag{6}$$

with the parameter space

$$\Theta_r = \mathcal{S}_r \times [0, +\infty) \tag{7a}$$

where

$$\mathcal{S}_r = \{ \boldsymbol{s} \in \mathcal{R}^m : \|\boldsymbol{s}\|_{\ell_0} \leq r \} \tag{7b}$$

is the sparse signal parameter space. The marginal likelihood function of $\boldsymbol{\theta}$ is obtained by *integrating* $\boldsymbol{z}$ *out* [see (5)]:

$$p_{\boldsymbol{y}\,|\,\boldsymbol{\theta}}(\boldsymbol{y}\,|\,\boldsymbol{\theta}) = \mathcal{N}(\boldsymbol{y}\,|\,H\,\boldsymbol{s}, \sigma^2\,H\,H^T) \tag{8a}$$

where the fact that H is a proper sensing matrix ensures that $H\,H^T$ is invertible. For a given sparsity level r, the maximum likelihood (ML) estimate of $\boldsymbol{\theta}$ is

$$\widehat{\boldsymbol{\theta}}_{\mathrm{ML}}(r) = \big(\widehat{\boldsymbol{s}}_{\mathrm{ML}}(r), \widehat{\sigma}^2_{\mathrm{ML}}(r)\big) = \arg\max_{\boldsymbol{\theta}\in\Theta_r} p_{\boldsymbol{y}\,|\,\boldsymbol{\theta}}\big(\boldsymbol{y}\,|\,\boldsymbol{\theta}\big). \tag{8b}$$

Obtaining the exact ML estimate $\widehat{\boldsymbol{\theta}}_{\mathrm{ML}}(r)$ in (8b) requires a combinatorial search and is therefore infeasible in practice. In the following, we present a computationally feasible algorithm that aims at maximizing (8a) and circumvents the combinatorial search.

ECME Hard Thresholding Algorithms For Known Sparsity Level r

We first review our ECME algorithm in [8] that approximately solves (8b). We assume that the sparsity level r known; consequently, we simplify the notation and omit the dependence of the estimates of $\boldsymbol{\theta}$ on r in this section. Here, we treat $\boldsymbol{z}$ as the *missing (unobserved) data* and maximize *either* the expected complete-data log-likelihood function (where the expectation is computed with respect to the conditional distribution of the unobserved data given the observed measurements) *or* the actual observed-data log-likelihood.

Assume that the parameter set estimate $\boldsymbol{\theta}^{(p)} = \big(\boldsymbol{s}^{(p)}, (\sigma^2)^{(p)}\big)$ is available, where p denotes the iteration index. *Iteration* $p+1$ of the ECME algorithm proceeds as follows:

- Update the sparse signal estimate using the expectation-maximization (EM) step, i.e. the expectation (E) step:

$$\boldsymbol{z}^{(p+1)} = \mathrm{E}_{\,\boldsymbol{z}\,|\,\boldsymbol{y},\,\boldsymbol{\theta}}[\boldsymbol{z}\,|\,\boldsymbol{y}, \boldsymbol{\theta}^{(p)}] = \boldsymbol{s}^{(p)} + H^T\,\big(H\,H^T)^{-1}\,(\boldsymbol{y} - H\,\boldsymbol{s}^{(p)}) \tag{9a}$$

  followed by the maximization (M) step:

$$\boldsymbol{s}^{(p+1)} = \mathcal{T}_r(\boldsymbol{z}^{(p+1)}\big); \tag{9b}$$

- update the variance-component estimate using the conditional maximization (CM) step:

$$(\sigma^2)^{(p+1)} = (\boldsymbol{y} - H\,\boldsymbol{s}^{(p+1)})^T\,(H\,H^T)^{-1}\,(\boldsymbol{y} - H\,\boldsymbol{s}^{(p+1)})/N. \tag{9c}$$

Here, $\mathrm{E}_{\,\boldsymbol{z}\,|\,\boldsymbol{y},\,\boldsymbol{\theta}}[\boldsymbol{z}\,|\,\boldsymbol{y}, \boldsymbol{\theta}]$ denotes the mean of the pdf $p_{\boldsymbol{z}\,|\,\boldsymbol{y},\,\boldsymbol{\theta}}(\boldsymbol{z}\,|\,\boldsymbol{y}, \boldsymbol{\theta})$.

In [9], we proposed the double overrelaxation (DORE) thresholding algorithm that accelerates the convergence of the ECME algorithm by interleaving two overrelaxation steps with the ECME steps. In the numerical examples, we will apply DORE and its automatic version described in the following section.

The empirical Bayesian signal estimate. We construct the following empirical Bayesian estimate of the random signal vector $\boldsymbol{z}$:

$$\mathrm{E}_{\boldsymbol{z}\,|\,\boldsymbol{y},\boldsymbol{\theta}}[\boldsymbol{z}\,|\,\boldsymbol{y},\boldsymbol{\theta}^{(+\infty)}] = \boldsymbol{s}^{(+\infty)} + H^T(HH^T)^{-1}(\boldsymbol{y} - H\boldsymbol{s}^{(+\infty)}). \tag{10}$$

where $\boldsymbol{\theta}^{(+\infty)} = (\boldsymbol{s}^{(+\infty)}, (\sigma^2)^{(+\infty)})$ denotes the estimate of the unknown parameter set upon convergence of the DORE iteration. Unlike $\boldsymbol{s}^{(+\infty)}$, the empirical Bayesian estimate (10) is not r-sparse in general, and is therefore preferable for reconstructing images that have nearly sparse transform coefficients. Observe that

$$\boldsymbol{y} = H\,\mathrm{E}_{\boldsymbol{z}\,|\,\boldsymbol{y},\boldsymbol{\theta}}[\boldsymbol{z}\,|\,\boldsymbol{y},\boldsymbol{\theta}^{(+\infty)}] \tag{11}$$

implying that the empirical Bayesian estimate (10) always achieves zero squared residual error (unlike $\boldsymbol{s}^{(+\infty)}$).

ADORE Algorithm for Unknown Sparsity Level

In [9], we proposed the automatic double overrelaxation (ADORE) algorithm for the case where the sparsity level r is unknown. ADORE aims at maximizing the following *unconstrained sparsity selection (USS)* objective function to select the appropriate r:

$$\mathrm{USS}(r) = -\tfrac{1}{2}\,r\,\ln\big(\frac{N}{m}\big) - \tfrac{1}{2}\,(N-r-2)\,\ln\Big(\frac{\widehat{\sigma}^2_{\mathrm{ML}}(r)}{\boldsymbol{y}^T\,(H\,H^T)^{-1}\,\boldsymbol{y}/N}\Big) \tag{12}$$

where $\widehat{\sigma}^2_{\mathrm{ML}}(r)$ is the ML estimate of the variance σ^2. Theorem 1 in [9] shows that, under appropriate conditions, the USS objective function optimally selects the sparsity level r that allows accurate signal representation and keeps as few nonzero signal elements as possible. Instead of the exhaustive search, ADORE applies the *golden-section search* with the initial search boundaries set to 0 and $\lceil N/2 \rceil$. For each candidate $0 < r \leq \lceil N/2 \rceil$, we estimate $\widehat{\sigma}^2_{\mathrm{ML}}(r)$ using the DORE iteration. The search process ceases when the searching interval becomes shorter than the prescribed resolution level L, see [9]. Therefore, ADORE requires roughly $1.4\,[\log_2(N/L) - 1]$ full DORE iterations. For the golden-section search to find the exact maximum of (12), $\mathrm{USS}(r)$ must be *unimodal* in r and DORE must converge to the ML estimate of $\boldsymbol{\theta}$, which is not true in general. Hence, ADORE maximizes (12) only approximately, yielding r_{ADORE}; then, our ADORE sparse-signal estimate is equal to the corresponding DORE estimate at $r = r_{\mathrm{ADORE}}$.

NDE X-RAY CT RECONSTRUCTION EXAMPLES

We now reconstruct an image of an industrial object from real X-ray CT measurements. We first compute the fast Fourier transforms (FFTs) of the CT projections and stack the real-valued FFT coefficients (separating the real and imaginary parts) of all projections into the measurement vector $\boldsymbol{y}$. By the Fourier slice theorem, the elements of $\boldsymbol{y}$ are the appropriate samples of the 2-D DSFT of the underlying image that lie on radial lines in the 2-D spatial frequency plane, see Fig. 1 and the discussion in the introduction of this paper. We implement the sampling matrix Φ in an efficient manner using the *nonuniform fast Fourier transform (NUFFT)* [10]. The $m \times m$ orthonormal sparsifying matrix Ψ is constructed using the *inverse Daubechies-6 wavelet matrix*. In this example, $m = 1024^2$ and N is equal to 1024 times the number of CT projections, which we vary in our experiments.

We consider three measurement scenarios that correspond to the frequency sampling patterns in Fig. 1. The sampling patterns in parts (a) and (b) of Fig. 1 correspond to the 180

(which is standard) and 90 uniform-angle X-ray CT projections, respectively. The sampling pattern in Fig. 1 (c) corresponds to a *limited-angle projection scenario* where 16 out of the 180 uniform projections are missing; the missing projections are contiguous in three regions.

We compare the traditional filtered backprojection (FBP) algorithm, DORE, ADORE with the search resolution set to $L = 500$, and the debiased gradient-projection for sparse reconstruction (GPSR) method in [11, Sec. III.B] with the convergence threshold $\texttt{tolP} = 10^{-5}$ and regularization parameter $\tau = 5 \cdot 10^{-5} \|H^T \boldsymbol{y}\|_{\ell_\infty}$ tuned for good reconstruction performance. For DORE and ADORE, we use the following convergence criterion:

$$\|\boldsymbol{s}^{(p+1)} - \boldsymbol{s}^{(p)}\|_{\ell_2}^2 / m < 10^{-14} \tag{13}$$

and estimate the transform coefficient vector $\boldsymbol{s}$ using the empirical Bayesian estimate (10), with $\boldsymbol{\theta}^{(+\infty)}$ equal to the parameter estimates obtained upon their convergence.

To implement DORE, we chose $r = 7000$. (Recall that DORE requires the knowledge of the signal sparsity level r.) In contrast, ADORE is *automatic* and estimates r from the measurements.

The left column of Fig. 2 shows the reconstruction results using the full 180 uniform projections. In this case, the DORE, ADORE and GPSR reconstructions in the second, third, and fourth row (respectively) are less grainy than the traditional FBP result in the first row.

The middle column of Fig. 2 shows the reconstruction results using 90 uniform projections. In this case, the FBP reconstruction contains strip-shaped artifacts (marked by arrows) that are caused by aliasing due to the undersampling. The DORE, ADORE, and GPSR reconstructions in the second, third, and last row (respectively) do not contain artifacts, but are slightly more blurred than the FBP result, particularly on the object boundary. In summary, DORE, ADORE, and GPSR exhibit a *graceful, artifact-free* degradation (loss in resolution) as the number of CT projections and the inspection time are halved compared with the full inspection: compare the left and middle columns of Fig. 2.

The right column of Fig. 2 shows the reconstruction results under the limited-angle projection scenario. In this case, FBP exhibits band artifacts (marked by arrows) that are caused by aliasing due to the missing projections. In contrast, DORE, ADORE, and GPSR are artifact-free and yield reconstructions that are very similar to those obtained from the full 180 uniform projections: compare the corresponding left and right columns of Fig. 2.

In all numerical examples, the ADORE method provides good reconstructions and demonstrates the effectiveness of our USS criterion. Recall that DORE and GPSR require tuning of sparsity related parameters and note that GPSR is sensitive to the choice of the tuning regularization parameter τ, see e.g. [9].

Table 1 shows the CPU times of the DORE, ADORE, and GPSR methods. In this example, DORE is significantly faster than GPSR. ADORE employs multiple DORE iterations to estimate the sparsity level and is the most time consuming.

CONCLUDING REMARKS

We applied our ECME hard thresholding algorithms for sparse signal reconstruction to a real X-ray CT scan and showed that, by exploiting the sparsity of the wavelet coefficients of the underlying images, we can avoid aliasing artifacts due to the undersampling and missing projections.

Further research will include developing hard thresholding methods for reconstructing sparse non-negative images.

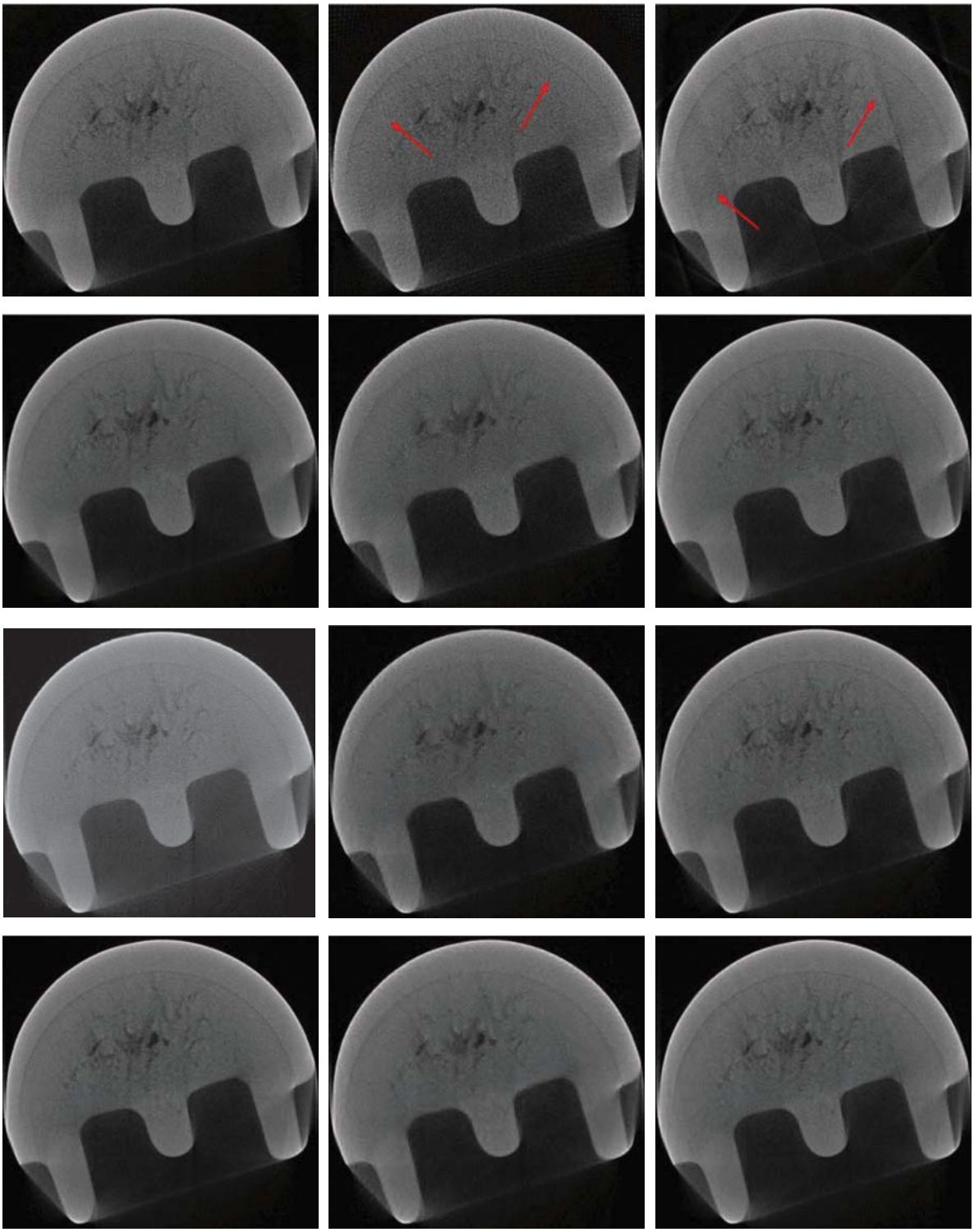

FIGURE 2. (First row) FBP, (second row) DORE, (third row) ADORE, and (fourth row) GPSR reconstructions from (left column) 180 uniform-angle projections, (middle column) 90 uniform-angle projections, and (right column) 164 limited-angle projections with sampling patterns in Fig.1.

TABLE 1. The CPU times of the DORE, ADORE, and GPSR methods in minutes.

	180 proj.	90 proj.	164 limited-angle proj.
DORE	7.1	8.7	11.0
GPSR	108.4	176.0	112.0
ADORE	736.5	500.6	706.3

ACKNOWLEDGMENT

This work was supported by the National Science Foundation under Grant CCF-0545571 and NSF Industry-University Cooperative Research Program, Center for Nondestructive Evaluation (CNDE), Iowa State University. We are grateful to Dr. J.N. Gray, CNDE, Iowa State University, for valuable discussions and for providing the experimental X-ray CT data.

REFERENCES

1. E.J. Candès, J. Romberg, and T. Tao, "Robust uncertainty principles: Exact signal reconstruction from highly incomplete frequency information," *IEEE Trans. Inform. Theory*, **52**, pp. 1207–1233 (2006).
2. E. Candès and J. Romberg, "Signal recovery from random projections," in *Computational Imaging III: Proc. SPIE-IS&T Electronic Imaging,* vol. 5674, C.A. Bouman and E.L. Miller (Eds.), San Jose, CA, (Jan. 2005), pp. 76–86.
3. E.J. Candès and J. Romberg, "Sparsity and incoherence in compressive sampling," *Inverse Problems*, **23**, pp. 969-985, (2007).
4. *IEEE Signal Processing Mag. Special Issue on Sensing, Sampling, and Compression*, (Mar. 2008).
5. M.F. Duarte *et al*., "Single-pixel imaging via compressive sampling," *IEEE Signal Processing Mag.*, **25**, pp. 83–91, (2008).
6. W.L. Chan *et al*., "A single-pixel terahertz imaging system based on compressed sensing," *Appl. Phys. Lett.*, **93**, (2008).
7. A.C. Kak and M. Slaney, *Principles of Computerized Tomographic Imaging*, New York: IEEE Press, (1988).
8. A. Dogandžić and K. Qiu, "Automatic hard thresholding for sparse signal reconstruction from NDE measurements," in *Rev. Progress Quantitative Nondestructive Evaluation*, D.O. Thompson and D.E. Chimenti (Eds.), Melville NY: Amer. Inst. Phys., vol. 29, (2010), pp. 806–813.
9. K. Qiu and A. Dogandžić, "Double overrelaxation thresholding methods for sparse signal reconstruction," in *Proc. 44th Annu. Conf. Inform. Sci. Syst.*, Princeton, NJ, (Mar. 2010).
10. J.A. Fessler and B.P. Sutton, "Nonuniform fast Fourier transforms using min-max interpolation," *IEEE Trans. Signal Processing*, **51**, pp. 560–574, (2003).
11. M.A.T. Figueiredo, R.D. Nowak, and S.J. Wright, "Gradient projection for sparse reconstruction: application to compressed sensing and other inverse problems," *IEEE J. Select. Areas Signal Processing*, **1**, pp. 586–597 (2007).